



Spectroscopic and kinetic responses of Cu-SSZ-13 to SO₂ exposure and implications for NO_x selective catalytic reduction



Arthur J. Shih^a, Ishant Khurana^a, Hui Li^b, Juan González^{a,c}, Ashok Kumar^d, Christopher Paolucci^{b,e}, Trevor M. Lardinois^a, Casey B. Jones^a, Jonatan D. Albarracín Caballero^a, Krishna Kamasamudram^d, Aleksey Yezerets^d, W. Nicholas Delgass^a, Jeffrey T. Miller^a, Aída Luz Villa^c, William F. Schneider^{b,*}, Rajamani Gounder^{a,*}, Fabio H. Ribeiro^{a,*}

^a Charles D. Davidson School of Chemical Engineering, Purdue University, 480 Stadium Mall Drive, West Lafayette, IN 47907, USA

^b Department of Chemical and Biomolecular Engineering, University of Notre Dame, Notre Dame, IN 46556, USA

^c Environmental Catalysis Research Group, Chemical Engineering Department, Engineering Faculty, Universidad de Antioquia, Calle 70, No. 52-21, Medellín, Colombia

^d Cummins Inc., 1900 McKinley Avenue, MC 50183, Columbus, IN 47201, USA

^e Department of Chemical Engineering, University of Virginia, 102 Engineer's Way, Charlottesville, VA 22904, USA

ARTICLE INFO

Keywords:

Cu-SSZ-13

Kinetics

NO_x selective catalytic reduction

sulfur poisoning

SO₂

ABSTRACT

The effects of sulfur poisoning on Cu-SSZ-13 zeolites, used commercially for the selective catalytic reduction (SCR) of nitrogen oxides (NO_x) with ammonia, were studied by exposing model Cu-zeolite powder samples to dry SO₂ and O₂ streams at 473 and 673 K, and then analyzing the surface intermediates formed using spectroscopic and kinetic assessments. Model Cu-SSZ-13 zeolites were synthesized to contain distinct Cu active site types, predominantly either divalent Cu²⁺ ions exchanged at proximal framework Al (Z₂Cu), or monovalent CuOH⁺ complexes exchanged at isolated framework Al (ZCuOH). SCR turnover rates (473 K, per Cu) decreased linearly with increasing S content to undetectable values at equimolar S:Cu ratios, consistent with poisoning of each Cu site with one SO₂-derived intermediate. Cu and S K-edge X-ray absorption spectroscopy and density functional theory calculations were used to identify the structures and binding energies of different SO₂-derived intermediates at Z₂Cu and ZCuOH sites, revealing that bisulfates are particularly low in energy, and residual Brønsted protons are liberated at Z₂Cu sites as bisulfates are formed. Molecular dynamics simulations also show that Cu sites bound to one HSO₄⁻ are immobile, but become liberated from the framework and more mobile when bound to two HSO₄⁻. These findings indicate that Z₂Cu sites are more resistant to SO₂ poisoning than ZCuOH sites, and are easier to regenerate once poisoned.

1. Introduction

Sulfur levels in diesel fuel were regulated by the Environmental Protection Agency (EPA) in 1993 to “low-sulfur” contents (500 ppm), and further in 2006 to “ultra-low sulfur” diesel fuel (15 ppm) [1]. Sulfur oxides (SO_x, x = 2, 3) formed during the combustion of diesel fuel deactivate Cu-SSZ-13 zeolite catalysts, which are used for the selective catalytic reduction (SCR) of nitrogen oxides (NO_x, x = 1, 2) with ammonia (NH₃-SCR). The “standard” SCR reaction stoichiometry is:



High temperature (673–1073 K) regeneration is a typical strategy used to reverse the deactivation of SO_x-poisoned Cu-SSZ-13 zeolites. A molecular understanding of how different Cu site types in Cu-SSZ-13

zeolites respond to sulfur exposure would aid in improving strategies to regenerate sulfur-poisoned materials and in developing catalysts that are more sulfur-tolerant [2–4].

Both physical and chemical processes have been invoked to explain sulfur deactivation of Cu-zeolites for NO_x SCR. In Fig. 1, we summarize the reported decreases in Cu-zeolite micropore volume as a function of sulfur content following various sulfur exposure conditions as collected from the literature. Ham et al. [5–7] reported a decrease in NO_x conversion during NH₃-SCR, and a concurrent decrease in the BET-derived surface area as measured by N₂ adsorption, with increasing sulfur content on Cu-MOR catalysts. Wijayanti et al. [8] (Cu-SAPO-34) and Brookshear et al. [9] (Cu-SSZ-13) reported similar observations on Cu-CHA exposed concurrently to SO₂ and NH₃, and this evidence has been used to support the proposal that pore-blocking by sulfur-derived

* Corresponding authors.

E-mail addresses: w Schneider@nd.edu (W.F. Schneider), rgounder@purdue.edu (R. Gounder), fabio@purdue.edu (F.H. Ribeiro).

<https://doi.org/10.1016/j.apcata.2019.01.024>

Received 3 December 2018; Received in revised form 14 January 2019; Accepted 27 January 2019

Available online 29 January 2019

0926-860X/© 2019 Elsevier B.V. All rights reserved.

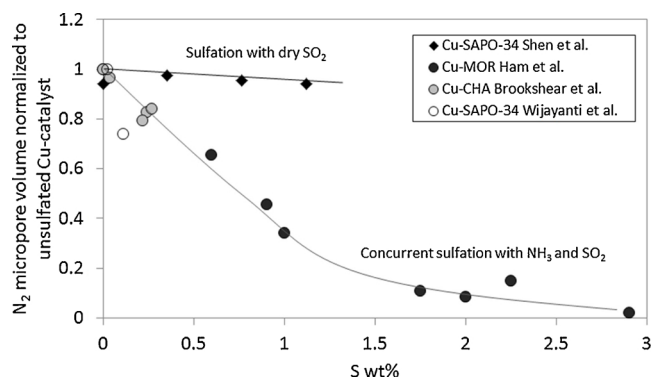


Fig. 1. Normalized micropore volume (BET-surface areas derived from N_2 adsorption) with increasing S content reported by Ham et al. [5], Brookshear et al. [9], Wijayanti et al. [8], and Shen et al. [10] when Cu-zeolites are poisoned with SO_2 , or with SO_2 and NH_3 concurrently.

species is the dominant mechanism of sulfur poisoning. In contrast, the BET-derived surface areas of Cu-SAPO-34 exposed only to SO_2 (in the absence of NH_3) is not observed to decrease with increasing sulfur content, leading Shen et al. to propose that sulfur-derived species adsorbed at Cu sites cause inhibition or deactivation [10]. Temperature programmed desorption (TPD) experiments reveal that Cu-zeolites store significantly more SO_2 than do H-form zeolites [10–12].

SO_2 and other molecules relevant to NH_3 -SCR catalysis, such as O_2 or NH_3 , may have a concurrent effect on the poisoning of Cu-zeolite catalysts. Oxidation catalysts upstream of the SCR catalyst in diesel exhaust aftertreatment systems oxidize SO_2 to SO_3 , with the fraction of SO_3 reported to increase with temperature until thermodynamic equilibrium between SO_2 , O_2 , and SO_3 is reached [13–15]. Cheng et al. [16] reported that SO_3 deactivates a Cu-zeolite catalyst (framework not specified) to a greater extent than does SO_2 alone. X-ray photoelectron spectroscopy (XPS) shows that the surface sulfur species are in the 6+ oxidation state after sulfation, regardless of whether SO_3 was present or not during poisoning treatments [16]. Hammershøi et al. [17] and Wijayanti et al. [18] demonstrated that total sulfur storage on Cu-CHA materials during SO_2 dosing increases in the presence of H_2O , NH_3 , and NO_x . Observed S:Cu ratios are greater on Cu-SAPO-34 materials exposed to SO_2 and NH_3 -SCR gases at low temperature (< 573 K) than when exposed to SO_2 , O_2 and H_2O at higher temperatures (> 573 K) [19].

Cu-CHA catalysts often only partially recover NH_3 -SCR reactivity after desulfation [11,12,14,20,21]. Hammershøi et al. report that SCR rates (per mass, 2–30% NO_x conversion) on Cu-SSZ-13 catalysts recover to only ~80% following repeated desulfation treatments under NH_3 -SCR conditions (823 K) [17]. Desulfation under these NH_3 -SCR conditions occurs only at temperatures greater than 573 K, consistent with sulfur desorption temperatures from TPD experiments [11,16,17,21,22]. Kumar et al. [23] and Ando et al. [24] demonstrated that desulfation occurs more readily in reducing environments ($NO + NH_3$, NH_3 , C_3H_6 , $n-C_{12}H_{16}$) than in oxidizing environments, enabling catalyst regeneration at more moderate temperatures. These authors proposed that redox cycling of Cu from the 2+ to 1+ oxidation state promotes regeneration of sulfur-poisoned Cu sites. In contrast, temperatures up to 823 K are required to regenerate Cu under the more oxidizing conditions of standard NH_3 -SCR.

Three major conclusions have emerged regarding the NH_3 -SCR reaction mechanism on sulfur-free Cu-SSZ-13 catalysts: (1) NH_3 -SCR involves a Cu^{2+}/Cu^+ redox process, (2) at low temperatures (< 573 K), the SCR active sites are derived from isolated Cu cations that are exchanged at anionic Al sites in the zeolite framework, and (3) the pool of

isolated Cu cation sites includes those present as $CuOH^+$ (ZCuOH) and Cu^{2+} (Z_2Cu) that are respectively charge compensated by one and two framework Al centers [25–30]. Cu^{2+}/Cu^+ redox cycling is supported using in operando X-ray absorption spectroscopy (XAS) to observe both Cu(I) and Cu(II) during standard NH_3 -SCR [29,31]. The redox cycle involves binuclear Cu-oxo complexes formed from mononuclear NH_3 -solvated Cu(I) sites during low temperature (< 573 K) NH_3 -SCR [31,32]. The evidence for two distinct mononuclear Cu(II) site types in Cu-SSZ-13 includes infrared spectroscopy (DRIFTS, FTIR) observation and quantification of the $\nu(O-H)$ stretching vibration at 3660 cm^{-1} of $CuOH^+$ sites, H_2 -temperature programmed reduction (H_2 -TPR), Rietveld refinement of X-ray diffraction patterns [33–35], and Cu:H⁺ site exchange stoichiometries. From these characterization studies, Cu ions preferentially exchange in SSZ-13 as Z_2Cu to saturation, and then as ZCuOH [30].

Luo et al. [35] and Jangjou et al. [21,35,36] compared the effects of sulfur exposure on Z_2Cu and ZCuOH sites. Luo et al. reported that the framework vibrational mode associated with ZCuOH (950 cm^{-1}) is completely suppressed following sulfur exposure, while the Z_2Cu mode (900 cm^{-1}) decreases to a lesser extent, implying that the former are more susceptible to sulfur poisoning than are the latter [35]. Jangjou et al. used in situ DRIFTS of Cu-SAPO-34 and NO as a probe molecule to conclude that ZCuOH sites deactivate through chemical poisoning and Z_2Cu sites via pore blocking [20]. They further develop kinetic models that incorporate different poisoning species on the two site types [36].

Here, we build on this prior work to isolate the effects of SO_2 exposure alone on ZCuOH and Z_2Cu sites in Cu-SSZ-13 zeolites, by combining an approach that interprets changes in NH_3 -SCR kinetic parameters with varying sulfur content, structural characterization of surface species using spectroscopy (XAS, UV-vis, FTIR), Brønsted acid site titration (NH_3) methods, and density functional theory (DFT) calculations. Kinetic measurements (reaction rate, reaction orders, and apparent activation energies) provide insights on the effects of sulfur poisoning and regeneration on ZCuOH and Z_2Cu sites. We find that the sulfur transforms both ZCuOH and Z_2Cu sites to inactive states, resulting in a constant SCR turnover rate when normalized by the number of residual Cu sites that are not poisoned by sulfur. We use DFT calculations and first-principles thermodynamics to compare poisoning intermediates as a function of exposure conditions that highlight chemical differences between the two Cu site types, including differences in the number of titratable Brønsted acid sites that can be detected in experiments.

2. Experimental

2.1. Synthesis, sulfation, and de-sulfation of Cu-zeolites

H-SSZ-13 zeolites were synthesized following a procedure reported by Fickel and Lobo [33], which is based on a patent by Zones [37]. The procedure was reported in our earlier publication [30]. SSZ-13 with Si:Al molar ratios of 4.5 and 25 were synthesized. The sodium form (Na-SSZ-13) was synthesized hydrothermally in a rotating oven at 433 K for 10 days, washed with water and acetone, then calcined at 823 K in dry air (AirZero, Indiana Oxygen) for 10 h to remove the template [29,38,39]. The resulting Na-SSZ-13 zeolite was converted to the NH_4 -form by ion exchange with 0.1 M NH_4NO_3 (> 99%, Sigma-Aldrich) (100 g solution per gram of catalyst) at 353 K for 10 h. The H-SSZ-13 zeolite was obtained by calcining the NH_4 -SSZ-13 at 823 K in dry air (AirZero, Indiana Oxygen) for 10 h.

Copper was exchanged onto H-SSZ-13 samples via aqueous-phase ion exchange with between 0 and 0.02 M solutions of $Cu(NO_3)_2$ (99.9% Sigma-Aldrich). During this process, NH_4NO_3 (> 99% Sigma-Aldrich) 0.1 M was added drop-wise to control the pH at a value of 5. The Cu-

SSZ-13 samples were dried at 373 K, cooled to room temperature under ambient air, then pelleted and sieved to retain 125–250 μm particles (W.S. TYLER No. 60 and No. 120 all-stainless-steel).

In this paper, two model catalysts were synthesized, one with a Si:Al of 4.5 with a Cu wt% of 3.8 (100% Z_2Cu , 0% ZCuOH) and one with a Si:Al of 25 with a Cu wt% of 1.5 (80% ZCuOH , 20% Z_2Cu). The relative fraction of Z_2Cu and ZCuOH active sites were confirmed using Cu elemental analysis and selective titration of Brønsted acid sites using NH_3 , as outlined in our previous publication [30]. Sulfation treatments were performed by saturating 0.5 g of sieved catalyst in a flowing stream of N_2 (600 mL min^{-1}) containing 100 ppm SO_2 at 473 K or 673 K for a pre-determined time, such that the cumulative molar exposure was S:Cu = 5. In this paper, sulfated sample names are preceded by 473 K SO_2 or 673 K SO_2 to denote sulfation treatments at 473 K and 673 K, respectively.

Desulfation treatments of sulfated samples were performed in a reductive environment in flowing N_2 (800 mL min^{-1}) containing of 500 ppm NH_3 and 500 ppm NO at 673 K. Typically, 0.02 to 0.05 g of each sulfated catalyst was heated to 673 K in dry nitrogen (liquid nitrogen boil-off, Linde) with a ramp rate of 283 K per minute, then exposed to flowing NH_3 and NO stream for a pre-determined time, such that the cumulative molar exposure of NO:S was 100. The de-sulfated catalysts were then cooled to ambient temperature in N_2 flow.

2.2. Catalyst characterization

Bulk Si, Al and Cu contents in all Cu-SSZ-13 samples were determined by atomic absorption spectroscopy (AAS) on a PerkinElmer AAnalyst[®] 300 atomic absorption spectrometer. For AAS sample preparation, 20–50 mg of sample was dissolved in 2 mL of hydrofluoric acid (HF, 48 wt%, Sigma-Aldrich) for 24 h. The dissolved sample was then diluted with 50–140 g of deionized H_2O (Millipore, 18.2 $\text{m}\Omega$).

Si, Al, Cu, and S were also measured using inductively coupled plasma — optical emission spectroscopy (ICP-OES) on an iCAP 7400 ICP-OES analyzer. Samples were prepared by acid microwave digestion. For ICP-OES sample preparation, about 30 mg of sample is transferred to a Teflon liner with 9 mL of HNO_3 , 3 mL HF, and a magnetic stir bar, then heated while stirring to 503 K (temperature reached in 5 min) and holding at 503 K for 20 min. Next, the sample was allowed to cool to ambient temperature for 1 h, after which point 10 mL of 4% boric acid was added. The sample was heated while stirring to 453 K in 4 min and held for 15 min. Once cooled, the resulting liquid was diluted to 100 mL.

Scanning electron microscopy images were collected using a FEI Quanta 3D FEG[®] scanning electron microscope. Electron dispersive X-ray analysis was used to determine the elemental content for Si, Al, Cu, and S. X-ray powder diffraction patterns between 4 and 40° 2 θ were obtained using a Rigaku Smart Lab[®] X-ray diffractometer with a Cu K(α) radiation source operated at 1.76 kW.

Selective NH_3 titration of Brønsted acid sites was used to quantify the number of Brønsted acid sites, as described in our previous publications [38,40]. Briefly, 500 ppm of NH_3 in balance N_2 is flown through the catalyst at 433 K until saturation, then a stream of 2% H_2O in balance N_2 is used to flush out NH_3 bound to Lewis acidic Cu sites until steady state. At this point, temperature-programmed desorption (TPD) is performed and the NH_3 :Al is determined from integrating and quantifying the TPD profile.

UV–vis-NIR spectroscopy was used to identify changes in the coordination of copper active sites in sulfated Cu-SSZ-13, as evidence of SO_2 binding to Cu species. Also, the formation of intermediate $\text{NH}_4\text{-SO}_x$ -like species was studied by collecting spectra after saturating the samples with 500 ppm NH_3 at 298 K and 473 K. UV–vis-NIR spectra from 4000 to 50,000 cm^{-1} and scan speed of 2000 $\text{cm}^{-1} \text{min}^{-1}$ were

collected on a Cary 5000[®] UV–vis-NIR spectrophotometer equipped with a Harrick-Scientific Praying-Mantis[®] diffuse reflectance optics and cell. BaSO_4 (99%, Sigma-Aldrich) was used as a 100% reflectance standard. All samples were dehydrated with 100 mL min^{-1} air (AirZero, Indiana Oxygen) at 523 K for 6 h before analysis. The low dehydration temperature of 523 K was selected to avoid desorption of sulfur species [11,16,17,21,22].

Argon (87 K) and nitrogen (77 K) micropore measurements were collected on a Micromeritics Accelerated Surface Area and Porosimetry (ASAP) 2020 system and were used to probe changes in accessible catalyst volumes after sulfation treatments. Prior to analysis, 15–30 mg of unsulfated Cu-SSZ-13 samples were degassed at 673 K under vacuum (< 5 μtorr) for 12 h and were compared to the same samples degassed at 423 K under vacuum (< 5 μtorr) for 4 h. Both degas treatments resulted in measurement of the same micropore volume within error, thus the lower temperature degas treatment was performed on the sulfated samples before collecting micropore volumes. Subjecting a sulfated sample to the 423 K degas treatment did not result in a significant decrease in sulfur content, as measured by ICP (Fig. S1).

Fluorescence sulfur K-edge X-ray absorption spectroscopy (XAS) was performed at Sector 9-BM of the Advanced Photon Source at Argonne National Laboratory. Samples were pressed into circular wafers (8 mm \times 0.5 mm thickness) and adhered to carbon tape, then transferred to a He-purged chamber to minimize losses in fluorescence signal. Energies were calibrated using a sodium thiosulfate pre-edge feature at 2469.20 eV. XAS spectra were collected in an energy range between 2420 and 2550 eV. Since sulfur content on all samples were low (< 1 wt%), dilution was not performed to minimize self-absorption. The sulfur content was not constant enough for quantitative analysis. XANES spectra are plotted as the ratio of the intensity of the total fluorescence signal to the intensity of the excitation radiation as a function of the photon energy. Pre-edge and post-edge spectra were normalized to 0 and 1, respectively.

Copper K-edge X-ray absorption spectroscopy (XAS) was performed at Sector 10-ID of the Advanced Photon Source at Argonne National Laboratory [41,42]. A Cu metal foil spectrum was simultaneously collected while measuring sample spectra to calibrate the Cu K-edge to 8979 eV. Operando and in situ experiments were performed in a glassy carbon reactor with catalyst diluted with spherical carbon beads to minimize beam absorption [25]. For operando XAS experiments, a standard SCR gas mixture was introduced to the reactor. H_2O was introduced into a N_2 (UHP, Airgas) and CO_2 (HP, Airgas) through a PermaPure MH[®] humidifier. Then, NO (3000 ppm in N_2 , Matheson Tri-Gas), O_2 (20% in He, Airgas) were added to the stream. NH_3 (3000 ppm in He, Matheson Tri-gas) was added last to minimize the formation of NH_4NO_3 . The reaction mixture was preheated to 473 K using preheater coil upstream of the reactor. For in situ XAS measurements under reducing conditions, 500 mL min^{-1} of a 300 ppm NO (3000 ppm in N_2 , Matheson Tri-Gas) and 300 ppm NH_3 (3000 ppm in He, Matheson Tri-gas) in balance N_2 was used. Again, the inlet flow was preheated to 473 K via heat tracing and a preheater coil. Sulfated catalysts were not calcined prior to exposure to gases and were not exposed to temperatures greater than 523 K to prevent desorption of sulfur species. For both operando and in situ experiments, concentrations were stabilized through a bypass before exposure to the catalyst bed. XAS spectra were collected in an energy range between 8700 and 9890 eV for samples held under different gas conditions, and between 8700 and 9780 eV for operando experiments. Once the catalyst was exposed to the gases, XAS spectra were taken approximately every 2 min until stabilization. NO_x , NH_3 , H_2O , CO_2 concentrations were measured using a Multi-Gas 2030[®] FTIR gas analyzer during operando and in situ experiments.

A method that quantifies only NH_3 adsorbed on Brønsted acid sites and Lewis acidic Cu sites, and not physisorbed on the zeolite structure,

was developed. The procedure involves saturation of the catalyst in a packed bed reactor with 500 ppm NH₃ in balance N₂ at 433 K (Fig. S2). On unsulfated samples, the NH₃:Al quantified from NH₃ consumption during the saturation step, and from NH₃ formation during the TPD step, were identical within error (Fig. S3). The parity in NH₃:Al measured during saturation and during TPD allow quantifying the ammonia stored on sulfated Cu-SSZ-13 materials without desorbing sulfur, which can damage downstream equipment.

2.3. SCR kinetic measurements

Kinetic measurements of NH₃-SCR were collected in a down-flow 3/8" ID tubular quartz reactor. Typically, 2–50 mg of sieved Cu-SSZ-13 catalyst were mixed with enough inert silica gel (Fisher Chemical Silica Gel (Davisil) Sorbent, Grade 923) to obtain a bed height of 7.05 cm. Aluminum foil was wrapped around the quartz reactor to an outer diameter of ~1 in. to enhance heat conduction and minimize radial and axial temperature gradients that may be present within the bed. The reactor was then placed within a clamshell furnace and pressure-tested with nitrogen (liquid nitrogen boil-off, Linde) at 5 psig for 20 min.

Steady state kinetic data were collected under differential NO conversions (below 20%) [43] and with products (H₂O and N₂) co-fed to ensure the entire bed was exposed to approximately the same gas concentrations and temperatures using a gas mixture of 300 ppm NO (3.5% NO/Ar, Praxair), 300 ppm NH₃ (3.0% NH₃/Ar, Praxair), 8% CO₂ (liquid, Indiana Oxygen), 10% O₂ (99.5%, Indiana Oxygen), 2.5% H₂O (deionized, introduced through 24" PermaPure MH Humidifier), and balance N₂ (boil-off liquid N₂, Linde) at 473 K and 1 atm. All concentrations are stabilized through the bypass prior to exposure to the catalyst bed. The gas hourly space velocity (GHSV) was varied between 600,000–4,000,000 h⁻¹ for all kinetic experiments while maintaining differential conversion. The fresh and sulfated catalysts were not calcined in dry air at elevated temperatures (~773 K) prior to collecting reaction kinetics due to sulfur desorption at temperature higher than 573 K. Dehydrating the catalyst with dry air at 523 K does not affect the SCR reaction rate (Fig. S4). In addition, continuous exposure to SCR gases between 423 and 523 K for 24 consecutive days did not affect the SCR reaction rate (Fig. S5). NO, NO₂, NH₃, CO₂, N₂O, and H₂O concentration data were recorded every 0.95 s using a MKS MultiGas 2030 gas-phase Fourier transform infrared (FTIR) spectrometer with on-board calibrations. Reaction temperatures were collected using two Omega[®] K-type 1/16" OD thermocouples with one placed in contact with the quartz wool above the top of the bed and the second placed in contact with the quartz frit below the bottom of the bed. The temperature difference was always within 3 K during steady state SCR catalysis. Total gas flow rates were measured using a soap bubble gas flow meter.

In the limit of differential NO conversion, the gas concentrations and catalyst bed temperature can be assumed constant, allowing the differential NO conversion rate to be calculated using Eq. (2):

$$-r_{NO} = \frac{(C_{NO,in} - C_{NO,out})}{1000000} \frac{P\dot{V}_{total}}{RT} \quad (2)$$

where C is the concentrations of NO in ppm before and after the catalyst bed, \dot{V}_{total} is the total volumetric flow rate, P is 1 atm, T is ambient temperature, and R is the gas constant. The experimental data are fitted to a power law rate expression (Eq. (3)) where k_{app} (Eq. (4)) is the apparent rate constant and α , β , γ , δ , and ϵ are the apparent reaction orders with respect to concentrations of NO, NH₃, O₂, H₂O, and CO₂, respectively.

$$-r_{NO} = k_{app} C_{NO}^{\alpha} C_{NH_3}^{\beta} C_{O_2}^{\gamma} C_{H_2O}^{\delta} C_{CO_2}^{\epsilon} \quad (3)$$

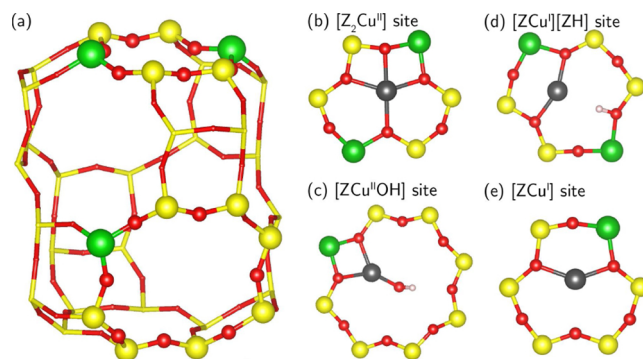


Fig. 2. Molecular structure of a SSZ-13 (CHA) cage, with the 1Al (ZCuOH) and 2Al (Z₂Cu) Cu sites on the right. Red, yellow, green, gray, and pink spheres correspond to O, Si, Al, Cu, and H atoms, respectively (For interpretation of the references to colour in this figure legend, the reader is referred to the web version of this article).

$$k_{app} = A_0 \exp\left(-\frac{E_{a,app}}{RT}\right) \quad (4)$$

All reported rates are free of external diffusion limitations (independent of space velocity) and internal diffusion limitations, evident in turnover rates that are similar for crystallite sizes ranging from 0.5 to 2.5 μm [30,39,44]. The low values for δ and ϵ shown in Tables S5 and S6, show that product inhibition is negligible, validating the use of Eq. (2).

2.4. DFT simulation details

Calculations were performed within periodic triclinic SSZ-13 supercell that contains 12 T-sites [30], consistent with our previous studies [30,31,39]. Fig. 2(a) shows the structure of one chabazite (CHA) cage with some atoms presented as spheres to highlight the ring structures. Fig. 2(b) shows the Z₂Cu site where 2 Al (“Z”) atoms were substituted in the 6-membered ring (6MR). Fig. 2(c) shows the ZCuOH site where 1 Al atom was substituted.

To locate the minimum energy structures reported here, we first performed ab initio molecular dynamics (AIMD) simulations at 473 K for 30 ps on candidate structures using the Car-Parrinello molecular dynamics software (CPMD) [45]. Calculations were performed within the Perdew-Becke-Erzenhof (PBE) generalized gradient approximation (GGA) [46–48], ions described with Vanderbilt ultrasoft pseudopotentials [49] and plane waves cut off at 30 Ry. Simulations were run in the canonical (NVT) ensemble with 0.6 fs timesteps. A Nose-Hoover thermostat was used to control temperature to 473 K. Low energy geometry snapshots were extracted from the trajectories and optimized to obtain the local minima energy and structure at 0 K. At least two low energy configurations were extracted from the trajectories and relaxed to ensure consistency. Subsequent geometry optimizations were performed within the Vienna Ab initio Simulation Package (VASP) software [50]. Plane wave cutoff was 400 eV and the Brillouin zone sampled at the Γ -point, as appropriate for a solid insulator. Electronic energies were converged to 10⁻⁶ eV and geometries relaxed until atomic forces were less than 0.01 eV Å⁻¹ using the hybrid screened-exchange method of Heyd-Scuseria-Erzenhof (HSE06) and D2 for dispersion corrections. Charge analysis was performed by the method of Bader, and reported normalized to Cu²⁺ and Cu⁺ references (Z₂Cu and ZCu). We report Bader charges as a superscript to Cu (i.e. Cu^I and Cu^{II}).

The relative mobility of the Cu centers was quantified by running 150 ps of AIMD within CPMD and following the method described in a previous publication [30]. In order to sample possible configurations

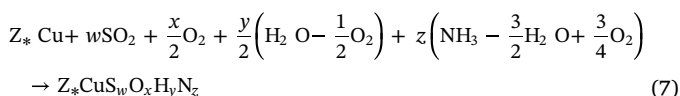
efficiently, we performed five independent 30 ps AIMD simulations starting from geometries slightly perturbed (maximum perturbation = 0.1 Å) from the equilibrium geometry. From each of the five simulations, 12 ps was used for equilibration and 18 ps was used for data collection.

We report the free energies of formation of various combinations of $S_wO_xH_yN_z$ on Cu sites with respect to SO_2 , O_2 , H_2O , and NH_3 :

$$\begin{aligned} \Delta G_{w,x,y,z}^{\text{form}}(T, \Delta\mu_{SO_2}, \Delta\mu_{O_2}, \Delta\mu_{H_2O}, \Delta\mu_{NH_3}) &= \Delta E_{w,x,y,z}^{\text{form}} - w\Delta\mu_{SO_2} - \frac{x}{2}\Delta\mu_{O_2} \\ &\quad - \frac{y}{2}\left(\Delta\mu_{H_2O} - \frac{1}{2}\Delta\mu_{O_2}\right) \\ &\quad - z\left(\Delta\mu_{NH_3} - \frac{3}{2}\Delta\mu_{H_2O} + \frac{3}{4}\Delta\mu_{O_2}\right) - T\Delta S(T) \end{aligned} \quad (5)$$

$$\begin{aligned} \Delta E_{w,x,y,z}^{\text{form}} &= E_{Z_*CuS_wO_xH_yN_z} - E_{Z_*Cu} - wE_{SO_2} - \frac{x}{2}E_{O_2} - \frac{y}{2}\left(E_{H_2O} - \frac{1}{2}E_{O_2}\right) \\ &\quad - z\left(E_{NH_3} - \frac{3}{2}E_{H_2O} + \frac{3}{4}E_{O_2}\right) \end{aligned} \quad (6)$$

where Z_*Cu ($*$ = 1,2) represents either a Cu bound near one Al or two Al placed as third nearest neighbors (3 NN) position in the 6MR. $\Delta E_{w,x,y,z}^{\text{form}}$ is the formation energy of reaction:



computed using the HSE06-D2 optimized energies of all species. To compute free energies, we neglect PV and heat capacity differences between the adsorbate-free and adsorbate-covered Cu sites and compute their entropy difference using a previously reported correlation derived from ab initio potential of mean force (PMF) free energy simulations [32], $\Delta_{\text{ads}}S^\circ = -0.35S_{\text{total}}^{\text{O},\text{i},\text{g}}$ for the ZCuOH site and $\Delta_{\text{ads}}S^\circ = -0.51S_{\text{total}}^{\text{O},\text{i},\text{g}}$ for the Z_2Cu site [30,51]. $\Delta\mu_{SO_2}$, $\Delta\mu_{O_2}$, $\Delta\mu_{H_2O}$, $\Delta\mu_{NH_3}$ are difference in ideal gas chemical potential (μ) between 0 K and the desired temperature (T) and pressure (P). We used the ΔH° and ΔS° values from the JANAF table [52] to calculate the $\Delta\mu$ at each discrete temperature (0 K, 100 K, etc., up to 1000 K), and linearly interpolated any other temperatures in between those discrete points.

3. Results and discussion

3.1. Characterization of SO_2 -exposed Z_2Cu and ZCuOH samples

Elemental analysis (AAS, ICP, EDS) of the model Cu-SSZ-13 catalysts before and after various SO_2 dosing treatments (600 mL min^{-1} of 100 ppm SO_2 in balance N_2 at 473 K or 673 K to reach a cumulative sulfur exposure of S:Cu = 5) are reported in Fig. 3. For a given exposure, the ZCuOH model catalyst stored more sulfur (per Cu) than the Z_2Cu model catalyst. The sulfur uptake increases with increasing sulfur exposure temperatures (Fig. 3), as also observed following SO_2 , O_2 and

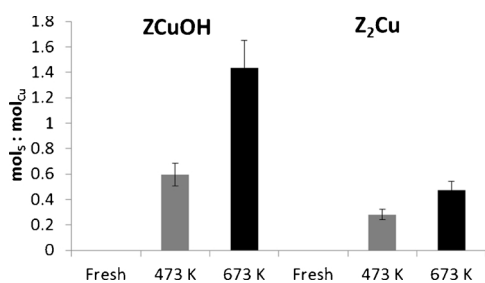
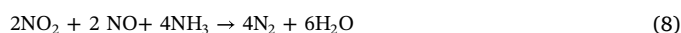


Fig. 3. Molar S:Cu ratios on model Cu-SSZ-13 samples following various SO_2 exposures.

H_2O dosing to Cu-SAPO-34 and Cu-SSZ-13 [19,53].

NH_3 -SCR kinetic parameters (apparent activation energies, apparent reaction orders) measured on the two model Cu-SSZ-13 samples at standard (10%) and excess (60%) O_2 feed compositions are reported in Table 1 (activation energy and reaction order plots for all samples can be found in Figs. S6–S27 and Tables S1–S6, Supp. Info.). Kinetic parameters (apparent activation energies, apparent reaction orders) collected at 10% O_2 (Table 1) suggest the ZCuOH and Z_2Cu samples to be operating in different rate-limiting regimes, complicating comparisons of their kinetic response to sulfur. In contrast, the apparent activation energy (~ 50 kJ mol^{-1}) and apparent NO orders (~ 1) are similar in 60% O_2 (Table 1), suggesting that O_2 is in kinetic excess and rates are limited by an NO + NH_3 reduction step in both samples [29,31,39]. Measurements made at these conditions provide more direct comparisons between the two samples. Fig. 4 shows the dependence of SCR rates (per Cu) and the apparent activation energy on S content for both model Cu-SSZ-13 samples. With increasing S content, the SCR rate (per Cu) decreases linearly to undetectable values at a S:Cu ratio of 1, while apparent activation energies appear constant (40–55 kJ mol^{-1}), suggesting equimolar poisoning of each Cu active site by an SO_2 -derived intermediate.

One ZCuOH sample adsorbed sulfur to an excess molar value of S:Cu of 1.4, and does not follow the equimolar poisoning behavior indicated by the dashed line in Fig. 4. This observation suggests sulfur to be present both as associated with Cu sites and adsorbed elsewhere on the sample. The E_{app} value of 14 kJ mol^{-1} on this sample is also much lower than on the other samples. The apparent activation energy and reaction orders on this sulfated sample are similar to those measured on a Cu-SSZ-13 sample that is volumetrically dilute in Cu (Cu wt% = 0.1 and Si:Al = 100, Table S7 and Figs. S28–S30), suggesting that sulfur may be effectively diminishing the ability of isolated Cu ions to form dimeric Cu intermediates during the SCR cycle. Thermogravimetric analysis (TGA) indicates that the ZCuOH sample poisoned to a S:Cu ratio of 1.4 contains a larger fraction of species that desorb at 1000 K than do other sulfated samples (Fig. S31). Under SCR conditions at 473 K, this sample is less than 100% selective to N_2 and is 20% selective towards NO oxidation to NO_2 (Fig. S32). This NO_2 generation and its subsequent consumption, for instance via fast SCR (Eq. (8)) on acid or Cu sites, makes it impossible to directly compare SCR kinetic parameters obtained on these materials with those on the other SO_2 -poisoned samples [54].



SCR rates (per Cu) decrease with S content on the two model Cu-SSZ-13 catalysts studied here, consistent with each S atom poisoning one ZCuOH or Z_2Cu site. Diffuse reflectance UV–vis spectra were collected on the model ZCuOH and Z_2Cu samples before and after sulfation treatments to identify electronic signatures correlated with sulfur uptake (Fig. 5). Spectra collected at ambient conditions (Fig. S33) are consistent with water-solvated Cu ions on both samples. Upon partial dehydration (523 K in dry air, to retain sulfur), however, qualitative differences in the d–d transition and charge transfer regions become apparent [28,30]. With increasing sulfur content, three of the four features in the d–d transition region disappear on the sample prepared to contain nominally ZCuOH sites, while the corresponding features in the sample prepared to contain nominally Z_2Cu sites are unchanged. Similarly, a new lower-energy feature in the charge transfer region (38,000 cm^{-1}) is more pronounced on the ZCuOH sample than the Z_2Cu sample. While the stoichiometric response to sulfur is similar on the two samples, the changes in UV–vis spectral features are not.

In situ and in operando XAS was used to probe qualitative changes in the Cu oxidation state following sulfation, because accurate quantification of Cu oxidation state in the presence of sulfur was not possible

Table 1

Apparent activation energies and reactant orders on unsulfated ZCuOH and Z₂Cu model catalysts collected under “10% O₂ SCR” conditions (300 ppm NO, 300 ppm NH₃, 10% O₂, 2.5% H₂O, 8% CO₂, balance N₂ at 473 K) and “60% O₂ SCR” conditions (300 ppm NO, 300 ppm NH₃, 60% O₂, 2.5% H₂O, 8% CO₂, balance N₂ at 473 K).

	E _{app} 10% O ₂ SCR	E _{app} 60% O ₂ SCR	NO order 10% O ₂ SCR	NO order 60% O ₂ SCR	O ₂ order 10% O ₂ SCR	O ₂ order 60% O ₂ SCR	NH ₃ order 10% O ₂ SCR	NH ₃ order 60% O ₂ SCR
ZCuOH	52	46	0.60	0.90	0.65	0.37	−0.40	−0.63
Z ₂ Cu	69	54	0.90	0.94	0.30	0.02	0.00	−0.04

(details in Supp. Info., Section S4). The fraction of Cu²⁺ that is reducible by exposure to NO and NH₃ decreases from 100% on the unsulfated samples to ~70% on all four sulfated samples (Table S9). Under reaction conditions from in operando XAS measurements, the Cu(II)/Cu(I) fraction is higher on sulfur-exposed ZCuOH samples than on sulfur-free ones. The Cu(II)/Cu(I) fraction is 0.9 on Z₂Cu samples even before sulfur exposure, so changes in response to sulfur could not be resolved (Table S8). From analysis of the EXAFS region, average Cu coordination numbers increased on ZCuOH materials and were unchanged on Z₂Cu materials following sulfation (Table S10). This observation corroborates the qualitative changes observed in UV–vis features of the ZCuOH sample, but not of the Z₂Cu sample, with increasing sulfur poisoning.

S K-edge XAS was used to probe the state of the sulfur species bound to the Cu sites. Ex situ XANES spectra were collected on the Z₂Cu and ZCuOH samples sulfated at either 473 K or 673 K, each of these samples exposed to 300 ppm NH₃ at 473 K for 1 h, and each of these samples exposed to standard SCR gas mix for 30 min. Fig. 6 plots all the normalized XANES spectra for the Z₂Cu samples (Fig. 6(a)) and the ZCuOH samples (Fig. 6(b)). All 12 spectra show a single prominent peak at 2480 eV, indicating the presence of S⁶⁺ species, regardless of sulfation and any subsequent gas treatment conditions. There is no other feature in between 2470 eV and 2477 eV, which rules out the presence of sulfur in other oxidation states (e.g. S^{2−} and S⁴⁺).

3.2. Characterization of desulfated Z₂Cu and ZCuOH samples

The four sulfated catalysts were desulfated in a NO + NH₃ feed stream (300 ppm NO, 300 ppm NH₃, balance N₂, 673 K) until a cumulative molar exposure of NO:S of 100 was obtained [23]. Elemental analysis results in Fig. 7 show that the sulfur content decreases by different proportions on each sample. Successive desulfation treatments were not performed due to experimental limitations on the amount of sample studied.

SCR reaction rates (per Cu) and activation energies measured on desulfated samples are shown in Fig. 8. Rates on Z₂Cu samples increase in direct proportion to the number of sulfur species removed, while the apparent activation energy and reaction orders are unchanged within error (Fig. 8, Fig. S50). Sulfation thus appears to result in the loss of

Z₂Cu active sites and to be reversible. In contrast, rates measured on desulfated ZCuOH samples do not recover to the original values after S content is accounted for, and apparent activation energies are also different before and after desulfation treatments, suggesting that some sites are irreversibly deactivated by sulfur. Reaction rates at a given S:Cu ratio on desulfated samples are higher on the ZCuOH catalyst that was initially poisoned to S:Cu > 1, than on the other catalysts, suggesting that desulfation may preferentially remove sulfur bound to the Cu over other types of sulfur species stored on the sample (Fig. S50).

We present quantitative evidence that, taken together, shows that sulfur poisons and deactivates both ZCuOH and Z₂Cu sites in an equimolar ratio at S:Cu < 1, but via mechanisms that reveal themselves differently in spectroscopic and pore volume measurements (N₂ and Ar micropore volume measurements and XRD data in Supp. Info., Section S5). Apparent activation energy and reaction orders are constant during the sulfation and desulfation processes. Turnover rates are constant when reaction rate is normalized to the number of initial Cu sites less the number of S species on each sample (mol_{Cu} − mol_S) (Fig. 9).

3.3. Structures and energies of sulfur species bound to Cu sites

We used DFT calculations and first-principles thermodynamics [30] to explore the differences in response of Z₂Cu and ZCuOH sites to exposure to SO₂, H₂O, O₂, and NH₃ as a function of temperature and exposure conditions. We drew on literature results [21,55,56] and chemical intuition to construct a variety of candidate structures containing up to two SO_x combined with NH₃ and H₂O, and then considered chemically relevant S/O/H compounds (SO₂, SO₃, sulfide, (bi)sulfite, (bi)sulfate) as ligands with and without OH, H₂O, NH₄⁺ and NH₃ ligands. We annealed using AIMD at 473 K and relaxed to obtain final DFT formation energies. All structures are provided as VASP CONTCAR files, and HSE06-D2 energies and normalized Bader charges are presented in the Supporting Information (Section S5, Tables S14 and S15).

Fig. 10 and 11 show the equilibrium phase diagrams for ZCuOH and Z₂Cu sites, respectively, as a function of NH₃ pressure and temperature at 20 ppm SO₂, 10% O₂, and 5% H₂O, 1 atm total pressure, chosen as variables to simplify presentation and to emphasize any differences

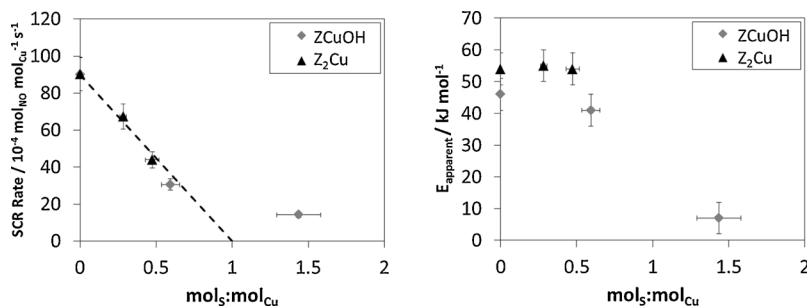


Fig. 4. Reaction rates and apparent activation energies for ZCuOH (diamonds) and Z₂Cu (triangles) model materials after sulfation. SCR conditions are 300 ppm NO, 300 ppm NH₃, 60% O₂, 2.5% H₂O, 8% CO₂, balance N₂ at 473 K.

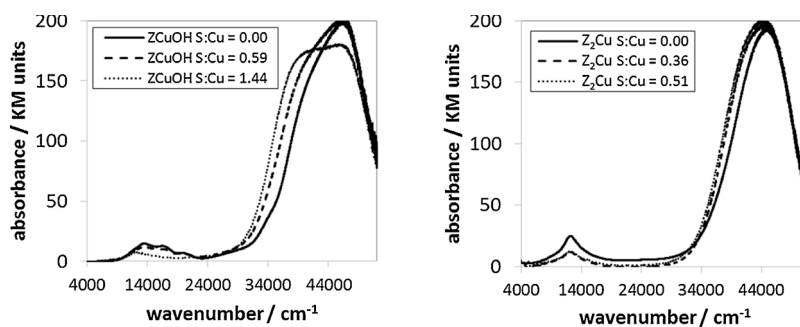


Fig. 5. Diffuse reflectance UV-vis spectra on ZCuOH (left) and Z_2Cu (right) after partial dehydration at 523 K under dry air.

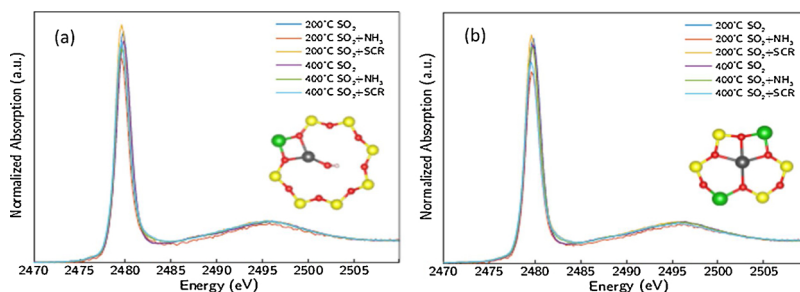


Fig. 6. Sulfur K-edge XANES measured ex situ at ambient conditions of ZCuOH (left) and Z_2Cu (right) samples treated with SO_2 and O_2 at either 200 °C or 400 °C. (For interpretation of the references to colour in this figure legend, the reader is referred to the web version of this article).

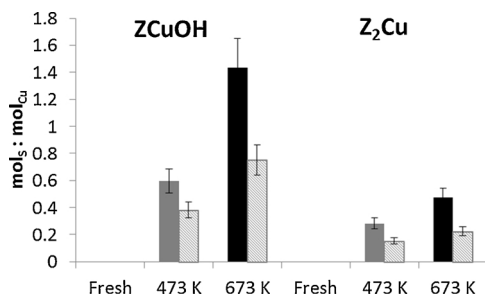


Fig. 7. S:Cu ratios before (solid bars) and after desulfation (hatched bars) on ZCuOH and Z_2Cu model materials.

between non-SCR and SCR conditions as a function of temperature. These diagrams report the thermodynamic equilibrium species without consideration of formation kinetics, and thus must be interpreted appropriately. Across the entire composition space, save for the highest temperature region of the ZCuOH diagram, Cu is present in the 2+ oxidation state, and all S species are present as bisulfate (HSO_4^-), consistent with the Cu and S oxidation states observed in the XAS above. Further, Cu^{2+} is always present in four-fold coordination consistent with EXAFS analysis (Section S4, Table S10). The left sides of the diagrams correspond to SO_2 exposure in the absence of NH_3 . In this limit, the most stable species on both Cu sites contain two bisulfate ligands at low temperature, transitioning to a single bisulfate at temperatures closer to those relevant to experimental dosing and consistent with the uptake stoichiometry of 1:1 S:Cu. The temperature to fully desorb sulfur is predicted to be upwards of 100 °C higher on ZCuOH than Z_2Cu . A key difference between the two sites is the predicted creation of a new Brønsted acid site upon sulfation for Z_2Cu but not ZCuOH.

To test this prediction, we employed methods we have developed previously to selectively quantify NH_3 adsorbed on Brønsted acid and Cu sites, while excluding physisorbed NH_3 [38,40]. Table 2 reports the number of excess NH_3 (per S), relative to the unsulfated Cu-SSZ-13

samples:

$$NH_3: S = \frac{(\text{mol } NH_3 \text{ on sulfated sample}) - (\text{mol } NH_3 \text{ on unsulfated sample})}{(\text{mol S on sulfated sample})} \quad (9)$$

Sulfation does not change the total number of NH_3 stored on the model ZCuOH catalyst, but does increase the amount of NH_3 stored in a ratio of 1 NH_3 :S for the model Z_2Cu catalyst (Table 2). The excess 1:1 NH_3 :S molar ratio on sulfated- Z_2Cu sites may reflect storage at excess Brønsted acid sites after sulfation, consistent with DFT predictions (Fig. 11) that the sulfation of Z_2Cu sites results in the generation of new Brønsted acid sites.

Moving to the right in Figs. 10 and 11, corresponding to increasing exposure to NH_3 , Z_2Cu sites eventually transition to an ammonium bisulfate and ZCuOH to an ammonium sulfate (regions 4 and 6, respectively). While absolute NH_3 pressures along this axis should be viewed cautiously due to the approximations used to capture the entropy of the products and uncertainties in the DFT energies themselves, it is clear that the ammonium species forms more readily on the Z_2Cu site than the ZCuOH. Further, it is clear that either in the absence or presence of NH_3 , sulfur species persist to higher temperature on ZCuOH than Z_2Cu sites, consistent with the experimentally observed trend in thermal desulfurization.

These results are consistent with an equivalent sulfur deactivation stoichiometry on the two sites and hint at differences in the deactivating species, but do not directly inform observed differences in deactivation mechanism. To test the effect of sulfur uptake on Cu mobility, we turned to AIMD calculations. We considered one and two bisulfate species on both Z_2Cu and ZCuOH sites, including species predicted to be stable near to the experimental conditions in the presence of NH_3 : $[ZCu^{II}(HSO_4)] [ZH]$ and $[Cu^{II}(HSO_4)_2] [Z_2H_2]$ on Z_2Cu and $[ZCu^{II}(HSO_4)]$ and $[Cu^{II}(HSO_4)_2] [ZH]$ on ZCuOH. We ran an extended period of AIMD as described in Section 2, and extracted the last 90 ps of the AIMD trajectory for further structural analysis. We estimated effective first shell coordination number (CN) from the computed radial distribution function (RDF) between Cu and all other heavy atoms

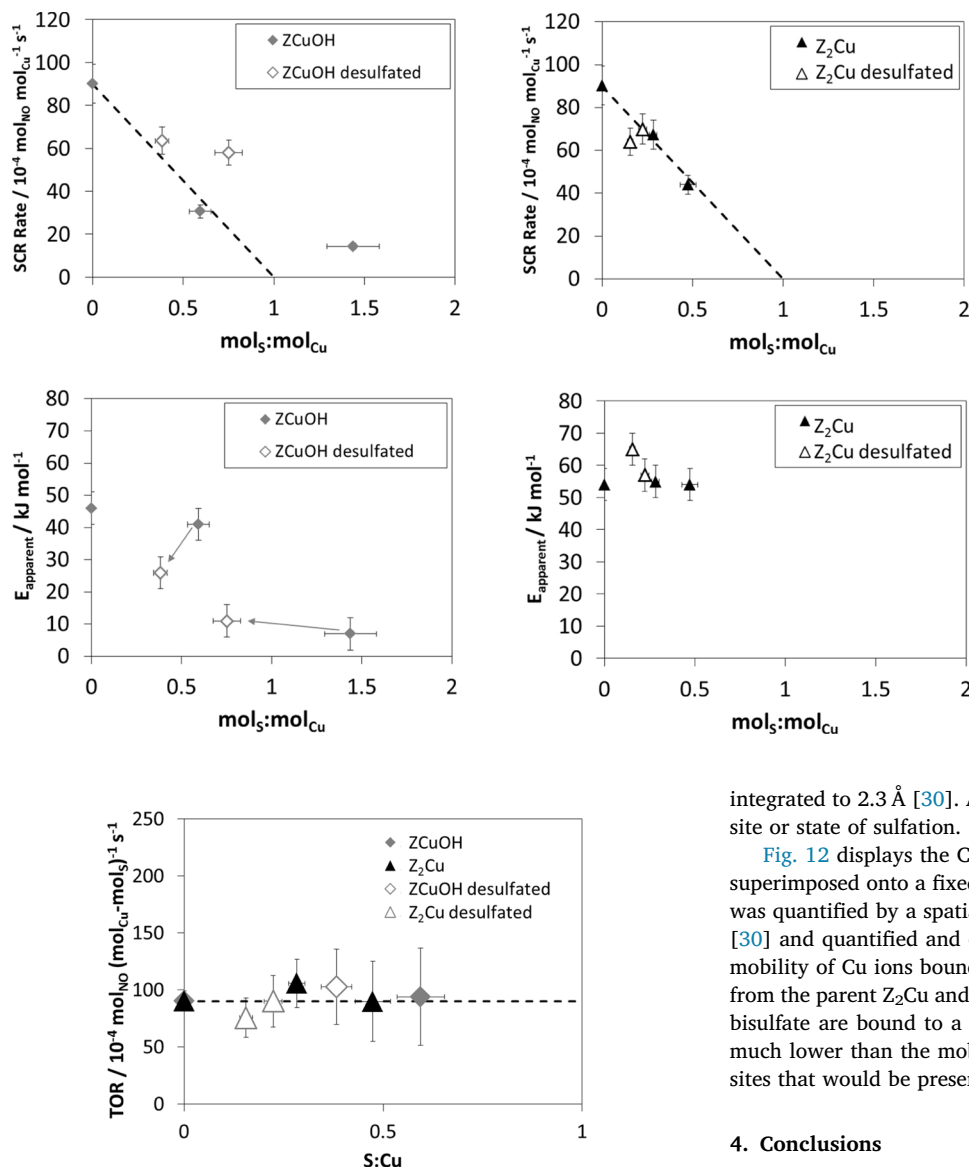


Fig. 9. Fresh, sulfated, and desulfated samples that exhibit the same apparent activation energy collapse to the same turnover rate when normalized to $(\text{mol}_{\text{Cu}} - \text{mol}_{\text{S}})$.

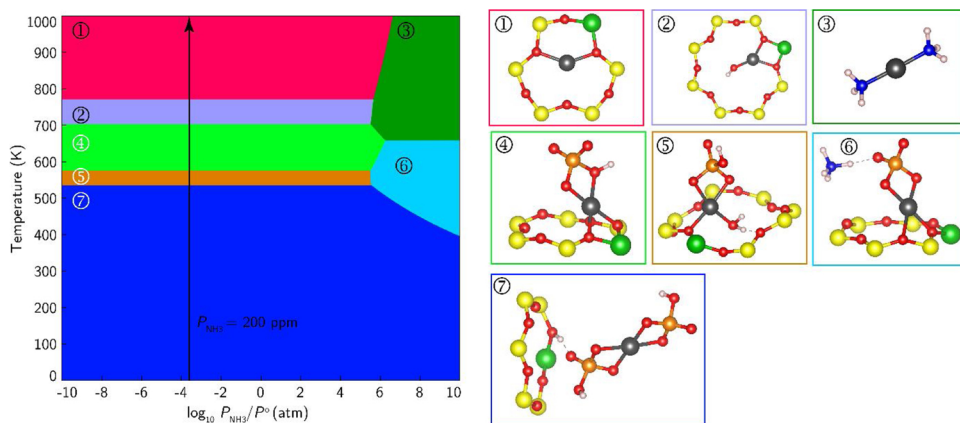


Fig. 8. Reaction rates and apparent activation energies for ZCuOH and Z_2Cu model materials after sulfation (filled) and desulfation (hollow). SCR conditions are 300 ppm NO, 300 ppm NH_3 , 60% O_2 , 2% H_2O , 8% CO_2 , balance N_2 at 473 K. Arrows indicate the starting and ending samples after desulfation, and thus how the apparent activation energy changes after desulfation.

integrated to 2.3 \AA [30]. As shown in Table 3, the CN is 4 regardless of site or state of sulfation.

Fig. 12 displays the Cu positions visited during the 90 ps of AIMD, superimposed onto a fixed zeolite framework. The relative Cu mobility was quantified by a spatial discretization method described previously [30] and quantified and compared to previous results in Table 3. The mobility of Cu ions bound to a single bisulfate are roughly unchanged from the parent Z_2Cu and ZCuOH sites and slightly increased when two bisulfate are bound to a Cu. The mobilities of all sulfated species are much lower than the mobilities of the NH_3 -solvated Z_2Cu and ZCuOH sites that would be present in the absence of sulfur (Table 3).

4. Conclusions

The effects of dry SO_2 poisoning at 473 and 673 K were determined on model Cu-SSZ-13 catalysts synthesized to contain nominally Cu^{2+} exchanged at proximal Al centers (Z_2Cu sites) or CuOH^+ exchanged at isolated Al centers (ZCuOH sites). ZCuOH sites are more prone to SO_2 -poisoning than Z_2Cu sites, reflected in the larger amounts of SO_2 -de-

Fig. 10. First-principles phase diagram for $\text{S}_w\text{O}_x\text{H}_y\text{N}_z$ species on a ZCuOH site vs temperature and NH_3 partial pressure at 1 atm total pressure and 20 ppm SO_2 , 10% O_2 , and 5% H_2O . Molecular structures corresponding to each region indicated by numbers. Gray, red, yellow, green, blue, orange, and white spheres correspond to Cu, O, Si, Al, N, S, and H atoms, respectively. Zeolite framework included only when directly hosting Cu or H (For interpretation of the references to colour in this figure legend, the reader is referred to the web version of this article).

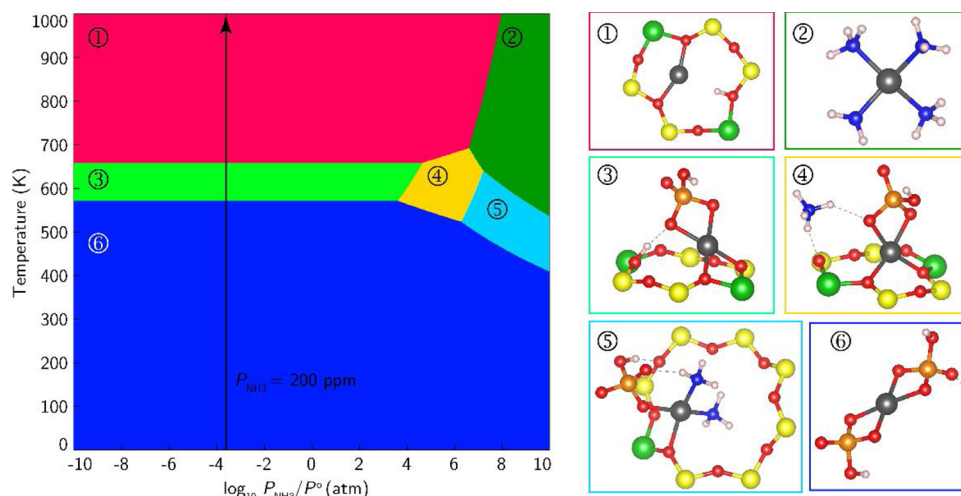


Fig. 11. First-principles phase diagram for $S_wO_2H_yN_z$ species on a Z_2Cu site vs temperature and NH_3 partial pressure at 1 atm total pressure and 20 ppm SO_2 , 10% O_2 , and 5% H_2O . Molecular structures corresponding to each region indicated by numbers. Gray, red, yellow, green, blue, orange, and white spheres correspond to Cu, O, Si, Al, N, S, and H atoms, respectively. Zeolite framework included only when directly hosting Cu or H (For interpretation of the references to colour in this figure legend, the reader is referred to the web version of this article).

Table 2

Molar NH_3 :S values calculated from excess NH_3 storage on Cu-SSZ-13 catalysts after dry SO_2 poisoning. Corresponding S:Cu loadings on the four samples and the total NH_3 :Cu molar ratios are also included for comparison.

Sample	NH_3 :S	S:Cu	NH_3 :Cu
ZCuOH	-0.2 ± 0.2	0.59	2.7
ZCuOH	0.0 ± 0.2	1.44	2.8
Z_2Cu	1.2 ± 0.2	0.36	3.0
Z_2Cu	0.9 ± 0.2	0.51	3.0

rived intermediates that were stored on the model ZCuOH sample than on the model Z_2Cu sample, upon exposure to the same sulfation treatment. NH_3 -SCR rates (473 K, per Cu) decrease proportionally with the S:Cu ratio on the Z_2Cu and ZCuOH samples, while apparent activation energies are essentially unaffected, consistent with equimolar Cu site poisoning by each SO_2 -derived intermediate. Additional SO_2 storage is also observed on non-Cu sites in the ZCuOH sample, and evidence is provided for partial micropore occlusion by SO_2 -derived species. Computation shows that bisulfates are particularly low in energy, that Z_2Cu and ZCuOH can take up one or two bisulfates, and that residual Brønsted acid sites are liberated as bisulfates are formed at Z_2Cu sites. Molecular dynamics simulations also show that Cu sites bound to one HSO_4 are immobile, but those bound to two are liberated from the framework and become more mobile. Taken together, experimental and theoretical characterizations support the hypothesis that Z_2Cu sites are more resistant to SO_2 poisoning than ZCuOH sites, and can be regenerated more easily once poisoned.

Table 3

Comparison of AIMD characterization of the 1Al/2Al samples, including composition of stable species, Cu-X (X = O, N) first shell coordination number (CN), average Cu-X bond distances (Å), and Cu mobility.

Condition	Sample	Chemical composition	CN	Avg. bond. Dist./Å	Cu mobility
Model sites (300 K) ^a	1Al	$[ZCu^{II}OH]$	3.0	1.96	1.1
	2Al	$[Z_2Cu^{II}]$	4.0	1.96	1.0
NH_3 -solvated (473 K) ^a	1Al	$Z[Cu^{II}(NH_3)_2]$	2.0	1.89	27.7
		$Z[Cu^{II}(OH)(NH_3)_3]$	4.0	2.05	18.2
	2Al	$Z[Cu^{II}(NH_3)_2][ZNH_4]$	2.0	1.89	13.4
		$Z_2[Cu^{II}(NH_3)_4]$	4.0	2.07	8.3
Sulfated (473 K) ^b	1Al	$[ZCu^{II}(HSO_4)]$	4.0	1.96	1.1
		$[ZH][Cu^{II}(HSO_4)_2]$	4.0	1.96	4.6
	2Al	$[ZH][ZCu^{II}(HSO_4)]$	4.0	1.98	1.7
		$[Z_2H_2][Cu^{II}(HSO_4)_2]$	4.0	1.96	2.6

^a Data from C. Paolucci, et al., J. Am. Chem. Soc., 138 (2016), 6028–6048. [30].

^b Data from this work.

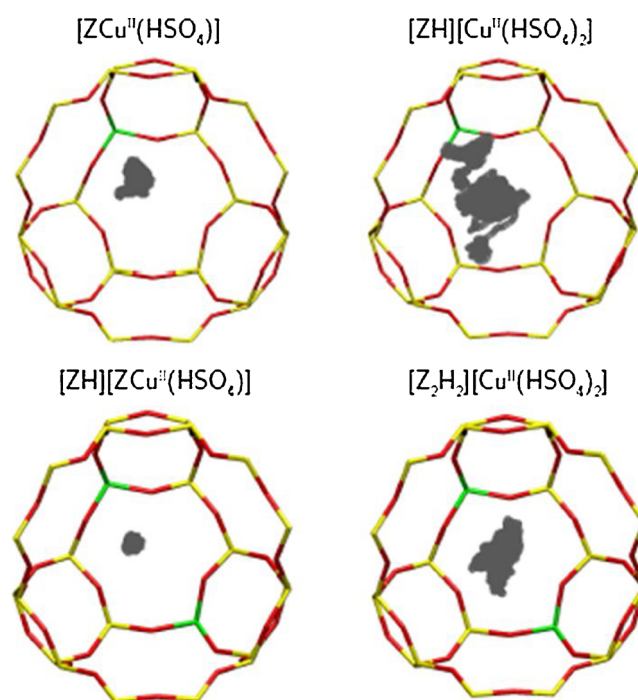


Fig. 12. Cu positions visited during 90 ps of AIMD at 473 K, represented by gray balls superimposed on a fixed zeolite framework. Framework was not constrained during the actual AIMD run.

Acknowledgements

First and foremost, we thank Chuck Peden for his guiding leadership and scientific insights to the automotive emissions catalysis community, and congratulate him on occasion of his 65th birthday. We acknowledge financial support provided by the National Science Foundation GOALI program under award numbers 1258715-CBET (Purdue) in support of experimental kinetics measurements and 1258690-CBET (Notre Dame) in support of theoretical calculations, and the National Science Foundation CAREER program under award number 1552517-CBET in support of experimental synthesis and characterization of the model catalyst samples. We also acknowledge the financial support provided by Cummins, Inc., and the Universidad de Antioquia and Purdue University through the Project CODI PURDUE-14 2-05. J.G. acknowledges the support from COLCIENCIAS, through the doctoral scholarship program, Call 647. We also thank Chuck Peden (PNNL), Feng Gao (PNNL), Janos Szanyi (PNNL), Jean-Sabin McEwen (Washington State) and their research groups for several fruitful technical discussions as part of our collaborative NSF GOALI project. We thank Atish Parekh (Purdue), John Di Iorio (Purdue) and the researchers in the Cummins Emissions Team for helpful technical discussions. We thank Michael J. Cordon for SEM and EDX measurements. We thank Sachem, Inc., for providing the organic structure-directing agent used to synthesize SSZ-13. We thank Tianpin Wu and Lu Ma from Sector 9-BM at the Advanced Photon Source for their assistance with S-edge XAS experiments in addition to Josh Wright from Sector 10 at the Advanced Photon Source for his assistance with Cu-edge XAS experiments.

Appendix A. Supplementary data

Supplementary material related to this article can be found in the online version, at doi:<https://doi.org/10.1016/j.apcata.2019.01.024>.

References

- [1] United States Environmental Protection Agency, Diesel Fuel Stand. (2017).
- [2] I. Bull, W. Xue, P. Burk, R.S. Boorse, W.M. Jaglowski, G.S. Koermer, A. Moini, J.A. Patchett, J.C. Dettling, M.T. Claude, U. S. Patent 7,601,662 B2 (2009).
- [3] J. Luo, K. Kamasamudram, N. Currier, A. Yezerets, Chem. Eng. Sci. 190 (2018) 60–67.
- [4] S. Dahlin, C. Lantto, J. Englund, B. Westerberg, F. Regali, M. Skoglundh, L.J. Pettersson, Catal. Today 320 (2019) 72–83.
- [5] S.W. Ham, H. Choi, I.S. Nam, Y.G. Kim, Ind. Eng. Chem. Res. 34 (1995) 1616–1623.
- [6] S.-W. Ham, I.-S. Nam, Y.G. Kim, Korean J. Chem. Eng. 17 (2000) 318–324.
- [7] M.H. Kim, I.S. Nam, Y.G. Kim, J. Catal. 179 (1998) 350–360.
- [8] K. Wijayanti, S. Andonova, A. Kumar, J. Li, K. Kamasamudram, N.W. Currier, A. Yezerets, L. Olsson, Appl. Catal. B 166–167 (2015) 568–579.
- [9] D.W. Brookshear, J.G. Nam, K. Nguyen, T.J. Toops, A. Binder, Catal. Today 258 (2015) 359–366.
- [10] M. Shen, H. Wen, T. Hao, T. Yu, D. Fan, J. Wang, W. Li, J. Wang, Catal. Sci. Technol. 5 (2015) 1741–1749.
- [11] A. Kumar, K. Kamasamudram, N. Currier, A. Yezerets, SAE Int. J. Engines 10 (2017) 9.
- [12] L. Zhang, D. Wang, Y. Liu, K. Kamasamudram, J. Li, W. Epling, Appl. Catal. B 156–157 (2014) 371–377.
- [13] A. Kumar, J. Li, J. Luo, S. Joshi, A. Yezerets, K. Kamasamudram, N. Schmidt, K. Pandya, P. Kale, T. Mathuraiveeran, Symp. Int. Automot. Technol. (2017).
- [14] A. Kumar, M.A. Smith, K. Kamasamudram, N.W. Currier, H. An, A. Yezerets, Catal. Today 231 (2014) 75–82.
- [15] T. Hamzehlouyan, C. Sampara, J. Li, A. Kumar, W. Epling, Top. Catal. 59 (2016) 1028–1032.
- [16] Y. Cheng, C. Lambert, D. Heui, J. Hun, S. June, C.H.F. Peden, Catal. Today 151 (2010) 266–270.
- [17] P.S. Hammershøi, Y. Jangjou, W.S. Epling, A.D. Jensen, T.V.W. Janssens, Appl. Catal. B Environ. 226 (2018) 38–45.
- [18] K. Wijayanti, K. Xie, A. Kumar, K. Kamasamudram, L. Olsson, Appl. Catal. B 219 (2017) 142–154.
- [19] P.S. Hammershøi, P.N.R. Vennestrøm, H. Falsig, A.D. Jensen, T.V.W. Janssens, Appl. Catal. B 236 (2018) 377–383.
- [20] Y. Jangjou, D. Wang, A. Kumar, J. Li, W.S. Epling, ACS Catal. 6 (2016) 6612–6622.
- [21] Y. Jangjou, Q. Do, Y. Gu, L.G. Lim, H. Sun, D. Wang, A. Kumar, J. Li, L.C. Grabow, W.S. Epling, ACS Catal. 8 (2018) 1325–1337.
- [22] Z. Zhang, J.D. Atkinson, B. Jiang, M.J. Rood, Z. Yan, Appl. Catal. B 164 (2015) 573–583.
- [23] A. Kumar, M.A. Smith, K. Kamasamudram, N.W. Currier, A. Yezerets, Catal. Today 267 (2016) 10–16.
- [24] R. Ando, T. Hihara, Y. Banno, M. Nagata, WCXTM 17 SAE World Congr. Exp. (2017).
- [25] V.F. Kispersky, A.J. Kropf, F.H. Ribeiro, J.T. Miller, Phys. Chem. Chem. Phys. 14 (2012) 2229–2238.
- [26] T.V.W. Janssens, H. Falsig, L.F. Lundegaard, P.N.R. Vennestrøm, S.B. Rasmussen, P.G. Moses, F. Giordano, E. Borfecchia, K.A. Lomachenko, C. Lamberti, S. Bordiga, A. Godiksen, S. Mossin, P. Beato, ACS Catal. 5 (2015) 2832–2845.
- [27] T. Günter, H.W.P. Carvalho, D.E. Doronkin, T. Sheppard, P. Glatzel, A.J. Atkins, J. Rudolph, C.R. Jacob, M. Casapu, J.-D. Grunwaldt, Chem. Commun. (Camb.) 51 (2015) 9227–9230.
- [28] F. Giordano, P.N.R. Vennestrøm, L.F. Lundegaard, F.N. Stappen, S. Mossin, P. Beato, S. Bordiga, C. Lamberti, Dalton Trans. 42 (2013) 12741–12761.
- [29] C. Paolucci, A.A. Verma, S.A. Bates, V.F. Kispersky, J.T. Miller, R. Gounder, W.N. Delgass, F.H. Ribeiro, W.F. Schneider, Angew. Chemie Int. Ed. 53 (2014) 11828–11833.
- [30] C. Paolucci, A.A. Parekh, I. Khurana, J.R. Di Iorio, H. Li, J.D. Albarracín Caballero, A.J. Shih, T. Anggara, W.N. Delgass, J.T. Miller, F.H. Ribeiro, R. Gounder, W.F. Schneider, J. Am. Chem. Soc. 138 (2016) 6028–6048.
- [31] C. Paolucci, I. Khurana, A.A. Parekh, S. Li, A.J. Shih, H. Li, J.R. Di Iorio, J.D. Albarracín-Caballero, A. Yezerets, J.T. Miller, W.N. Delgass, F.H. Ribeiro, W.F. Schneider, R. Gounder, Science 357 (2017) 898–903.
- [32] F. Gao, D. Mei, Y. Wang, J. Szanyi, C.H.F. Peden, J. Am. Chem. Soc. 139 (2017) 4935–4942.
- [33] D.W. Fickel, R.F. Lobo, J. Phys. Chem. C 114 (2010) 1633–1640.
- [34] J.H. Kwak, H. Zhu, J.H. Lee, C.H.F. Peden, J. Szanyi, Chem. Commun. (Camb.) 48 (2012) 4758–4760.
- [35] J. Luo, D. Wang, A. Kumar, K. Kamasamudram, N. Currier, A. Yezerets, Catal. Today 267 (2016) 3–9.
- [36] Y. Jangjou, C.S. Sampara, Y. Gu, D. Wang, A. Kumar, J. Li, W.S. Epling, React. Chem. Eng. (2019), <https://doi.org/10.1039/C8RE00210J>.
- [37] S.I. Zones, U. S. Patent No. 4,544,538 A (1985).
- [38] S.A. Bates, W.N. Delgass, F.H. Ribeiro, J.T. Miller, R. Gounder, J. Catal. 312 (2014) 26–36.
- [39] S.A. Bates, A.A. Verma, C. Paolucci, A.A. Parekh, T. Anggara, A. Yezerets, W.F. Schneider, J.T. Miller, W.N. Delgass, F.H. Ribeiro, J. Catal. 312 (2014) 87–97.
- [40] J.R. Di Iorio, S.A. Bates, A.A. Verma, W.N. Delgass, F.H. Ribeiro, J.T. Miller, R. Gounder, Top. Catal. 58 (2015) 424–434.
- [41] C.U. Segre, N.E. Leyarovsky, L.D. Chapman, W.M. Lavender, P.W. Plag, A.S. King, A.J. Kropf, B.A. Bunker, K.M. Kemner, P. Dutta, R.S. Duran, J. Kaduk, AIP Conf. Proc. 521 (2000) 419–422.
- [42] A.J. Kropf, J. Katsoudas, S. Chattopadhyay, T. Shibata, E.A. Lang, V.N. Zyryanov, B. Ravel, K. McIvor, K.M. Kemner, K.G. Scheckel, S.R. Bare, J. Terry, S.D. Kelly, B.A. Bunker, C.U. Segre, AIP Conf. Proc. 1234 (2010) 299–302.
- [43] H.A. Massaldi, J.A. Maymo, J. Catal. 14 (1969) 61–68.
- [44] R.M. Koros, E.J. Nowak, Chem. Eng. Sci. 22 (1967) 470.
- [45] CPMD, <http://www.cpmd.org/>, Copyright IBM Corp 1990–2016, Copyright MPI für Festkörperforschung Stuttgart 1997–2001.
- [46] J.P. Perdew, Y. Wang, Phys. Rev. 45 (1992) 244.
- [47] J.P. Perdew, K.A. Jackson, M.R. Pederson, D.J. Singh, C. Fiolhais, Phys. Rev. B 46 (1992) 6671.
- [48] J.P. Perdew, K. Burke, M. Ernzerhof, Phys. Rev. Lett. 77 (1996) 3865–3868.
- [49] K. Laasonen, A. Pasquarello, R. Car, C. Lee, D. Vanderbilt, Phys. Rev. B 47 (1993) 10142–10153.
- [50] G. Kresse, J. Furthmüller, Phys. Rev. B Condens. Matter Mater. Phys. 54 (1996) 11169–11186.
- [51] H. Li, C. Paolucci, W.F. Schneider, J. Chem. Theory Comput. 14 (2018) 929–938.
- [52] NIST-JANAF, <https://kinetics.nist.gov/janaf/>, Last Accessed: December 2, 2018.
- [53] P.S. Hammershøi, A.D. Jensen, T.V.W. Janssens, Appl. Catal. B 238 (2018) 104–110.
- [54] S. Li, Y. Zheng, F. Gao, J. Szanyi, W.F. Schneider, ACS Catal. 7 (2017) 5087–5096.
- [55] G. Yang, X. Du, J. Ran, X. Wang, Y. Chen, J. Phys. Chem. C 122 (2018) 21468–21477.
- [56] P.S. Hammershøi, Y. Jangjou, W.S. Epling, A.D. Jensen, T.V.W. Janssens, Appl. Catal. B 226 (2018) 38–45.